Kusiak, M. A., Kovaleva, E., Wirth, R., Klötzli, U., Dunkley, D. J., Yi, K., Lee, S. (2019): Lead oxide nanospheres in seismically deformed zircon grains. - *Geochimica et Cosmochimica Acta*, *262*, pp. 20—30.

DOI: http://doi.org/10.1016/j.gca.2019.07.026

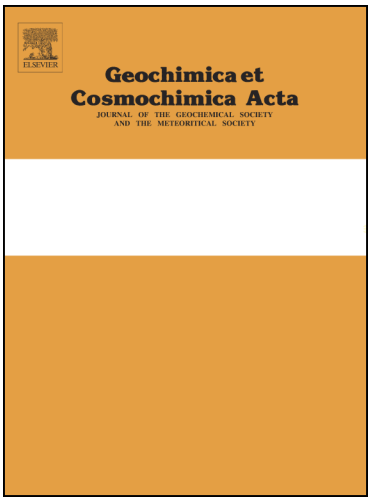

Lead oxide nanospheres in seismically deformed zircon grains

M.A. Kusiak, E. Kovaleva, R. Wirth, U. Klötzli, D.J. Dunkley, K. Yi, S. Lee

PII: S0016-7037(19)30450-8
DOI: https://doi.org/10.1016/j.gca.2019.07.026
Reference: GCA 11346

To appear in: *Geochimica et Cosmochimica Acta*

Received Date: 18 January 2019
Revised Date: 11 July 2019
Accepted Date: 12 July 2019

Please cite this article as: Kusiak, M.A., Kovaleva, E., Wirth, R., Klötzli, U., Dunkley, D.J., Yi, K., Lee, S., Lead oxide nanospheres in seismically deformed zircon grains, *Geochimica et Cosmochimica Acta* (2019), doi: https://doi.org/10.1016/j.gca.2019.07.026

Lead oxide nanospheres in seismically deformed zircon grains

Kusiak, M.A.[1,2], Kovaleva, E.[3], Wirth, R.[4], Klötzli, U.[5], Dunkley, D.J.[6], Yi, K.[7], Lee, S.[7]

[1]*Institute of Geophysics, Polish Academy of Sciences, Księcia Janusza 64 St., PL-01452 Warsaw, Poland; monika.kusiak@igf.edu.pl*

[2]*GeoForschungsZentrum Potsdam, Section 3.6 Chemistry and Physics of Earth Materials, D-14473 Potsdam, Germany*

[3]*University of the Free State, Department of Geology, 205 Nelson Mandela Drive, 9300 Bloemfontein, Free State, South Africa*

[4]*GeoForschungsZentrum Potsdam, Section 3.5 Surface Geochemistry, D-14473 Potsdam, Germany*

[5]*University of Vienna, Department of Lithospheric Research, 14 Althanstrasse, 1090 Vienna, Austria*

[6]*Faculty of Earth Sciences, University of Silesia, ul. Będzińska 60, PL-41205 Sosnowiec, Poland*

[7]*Division of Earth and Environmental Sciences, Korea Basic Science Institute, Chungcheongbukdo 28119, Republic of Korea*

Abstract

The presence of Pb oxide nanospheres in zircon from mylonites of the Ivrea-Verbano Zone (IVZ), Northern Italy is described for the first time. Isotopic dating of zircon reveals detrital cores with ages scattered from 960 to 320 Ma, and metamorphic rims with a mean age of 280 ± 4 Ma. Zircon crystals, derived from samples that contain pseudotachylite formed during seismic events, have planar fractures (PFs) and planar deformation bands (PDBs). The PDBs are associated with straight dislocation arrays in glide configuration. Detrital zircon cores have mottled diffraction contrast in TEM bright field images, indicative of irradiation damage and/or annealing in radiation damaged zircon. Lead oxide nanospheres up to 9 nm in diameter, as recognized in TEM, occur in detrital cores but not in metamorphic rims of the zircon. No relationship was observed between the nanospheres and PDBs or PFs. This is the first report of lead oxide nanospheres in zircon from a Phanerozoic metamorphic rock, as well as being the first observed case of such nanoinclusions being

composed of Pb oxide, rather than native Pb. The formation of the nanospheres is attributed to high-temperature metamorphism, with subsequent seismic activity having little effect on distribution or preservation.

1. INTRODUCTION AND RATIONALE OF THE STUDY

Although zircon is widely used in geochronology (Davis et al., 2003; Rubatto, 2017), the reliability and significance of isotopic data obtained from this common accessory mineral requires consideration of the potential complexity of internal structures within individual crystals, such as growth zoning, chemical/isotopic heterogeneity, and crystallinity (e.g. Bea et al., 2018; Corfu et al. 2013; Geisler et al., 2001; Nasdala et al. 2001, 2010; Piazolo et al. 2012; Seydoux-Guillaume et al., 2015). This is especially the case when rocks that contain zircon have been subjected to metamorphism and plastic and/or brittle deformation, which can induce chemical and isotopic redistribution in zircon crystals through a variety of mechanisms (Bea and Montero 2013; Kovaleva and Klötzli, 2017; Kusiak et al., 2013a;b; 2015; 2018; Peterman et al., 2016; Piazolo et al., 2016; Valley et al., 2014; 2015; Whitehouse et al., 2017). Since the abundance and spatial distribution of Pb isotopes is a particularly important parameter for U-Pb geochronology, it is crucial to understand how radiogenic Pb in zircon crystals is affected by heating and deformation (e.g. Kovaleva et al., 2017; Timms et al., 2011; 2012; Peterman et al., 2016).

Recently, it has been recognized that during metamorphism, radiogenic Pb can be mobilized in zircon to form either nanoclusters (Ge et al., 2018; Peterman et al., 2016; Piazolo et al., 2016; Valley et al., 2014) or Pb nanospheres (Kusiak et al., 2015; 2018; Whitehouse et al., 2017). Nanoclusters were detected by atom probe tomography (ATM) and are up to 10 nm in size (Peterman et al., 2016). It has been proposed that nanoclusters of Pb are formed around dislocation loops caused by radiation damage and that they possibly record the timing of metamorphism (Peterman et al., 2016; Reddy et al., 2016). Lead nanospheres, in contrast, have been documented only by transmission electron microscopy (TEM) and form metallic Pb. Examples of native lead nanoinclusions up to 35 nm in diameter have been attributed to thermal annealing of radiation-damaged zircon during granulite to ultra-high temperature metamorphism (Kusiak et al., 2015; 2018; Whitehouse et al., 2017).

According to Kovaleva and Klötzli (2017), lead can also be re-distributed in the presence of planar deformation bands (PDBs) in seismically-deformed zircon, forming clusters of 1-1.5 μm in diameter, as documented by high-resolution secondary ion mass spectroscopy (NanoSIMS) mapping. Planar deformation bands form in zircon as a result of crystal-plastic deformation under high-strain conditions (Kovaleva et al., 2015). Most zircon grains with PDBs are found in seismic environments (Kovaleva et al., 2015; Kovaleva and Klötzli, 2017), and also have been observed in shocked zircon from impactites (Erickson et al., 2013; 2016; Cavosie et al., 2018). The PDBs are rotated portions of crystal lattice characterized by straight (planar) boundaries, 0.5-3 μm in thickness and misoriented from the main part of host grain by 0.3 to 10°. Typical spacing of PDBs is around 5 μm, varying from <1 μm to 25 μm. It has been suggested by Kovaleva and Klötzli (2017) that the formation of PDBs can affect zircon isotopic ages, and zircon with PDBs might therefore be a potential tool for dating paleo-seismic events.

For the present study, zircon grains with PDBs observed by Kovaleva et al. (2015) were microstructurally characterized by TEM, in order to find out the nature of Pb clusters observed by Kovaleva and Klötzli (2017) and to determine if they are in fact Pb nanospheres as discovered by Kusiak et al. (2015) in zircons from high grade metamorphic rocks in Antarctica. The foils were taken from crystals to understand the relationship between the Pb concentration and PDBs. Further, the zircon population was isotopically analyzed by Sensitive High Resolution Ion Microprobe (SHRIMP) to measure isotopic ages in zircon detrital cores and metamorphic rims. We also aim to compare deformation microstructures within detrital cores and metamorphic rims of the same zircon population, as these domains experienced different geological histories and have different ages.

2. THE IVREA-VERBANO ZONE: GEOLOGICAL SETTING AND SAMPLES

The samples used in this study are mylonitic metapelite from the Ivrea-Verbano Zone (IVZ), derived from an outcrop by the village of Premosello in the Val d′Ossola, Southern Alps, Northern Italy (Fig. 1). The IVZ represents a section of lower continental crust that experienced thinning and high-temperature regional metamorphism during the uppermost Palaeozoic (Rutter et al., 2007). It consists of a steeply dipping, NE-SW trending succession of meta-sedimentary and meta-igneous

basic rocks, ultrabasic mantle tectonites and a large underplated mafic igneous complex (Brodie and Rutter, 1987; Brodie et al., 1989). The section is dominated by metasedimentary rocks in the SE part and by metabasic rocks in the NW part. Metamorphic grade increases progressively from amphibolite facies in the SE to granulite facies in the NW.

Mylonites from the sampling area in the northern part of the Ivrea-Verbano zone were formed under granulite-facies conditions during crustal extension and simultaneous magmatic underplating that occurred at 315-265 Ma (Rutter et al., 2007). Peak *P-T* conditions of the sampling area were estimated at 1.0–1.2 GPa and 800–900°C in metagabbro from Val d′Ossola (Pittarello et al., 2012; Redler et al., 2012). The emplacement of pseudotachylites (frictional melts) occurred after peak metamorphism at 550–650°C and 0.4–0.6 GPa (Pittarello et al. 2012). These frictional melts and related ultramylonites were formed at ca. 10 km depth as a result of high differential stresses and strain rates released by seismic slip and coeval shearing at elevated temperatures (Pittarello et al., 2008). Extended period of high-T metamorphism was suggested by various studies (e.g. Peressini et al., 2007; Guergouz et al., 2018; Kunz et al., 2018).

Felsic mylonitic metapelites are strongly restitic, dehydrated metasedimentary rocks re-equilibrated under granulite-facies conditions. They are composed of garnet porphyroblasts ranging from 50 to 500 μm in diameter hosted by foliated matrix consisting of alternating plagioclase and quartz-rich laminations, intercalated by biotite-ilmenite-rich laminations. The latter define a mylonitic foliation. Pseudotachylites occur as foliation-parallel dark-grey veins 2-3 mm thick, often offset and truncated by high-angle fractures. The veins are hosted by 1-2 cm thick dark ultramylonitic layers parallel to the main foliation. Both pseudotachylites and ultramylonites are composed of fine-grained matrix of mixed plagioclase, quartz, biotite, and ilmenite. Pseudotachylites contain internal rims of skeletal garnet and preserve needle-shaped microlites, ranging from 1 to 5 μm in length (Kovaleva et al., 2015). Deformed zircons from mylonitic metapelites of the IVZ that contain PDBs and planar fractures (PF) are hosted by ultramylonites, with a strong spatial association with pseudotachylitic veins (Pitarello et al., 2012; Kovaleva et al., 2015).

3. METHODOLOGY

3.1 Cathodoluminescene and orientation contrast imaging

Zircon grains were identified and characterized by cathodoluminescence (CL) imaging in order to reveal internal growth features, using a FEI Inspect S scanning electron microscope equipped with a Gatan MonoCL detector, at the Faculty of Geosciences, Geography and Astronomy, University of Vienna, Austria. Imaging was done with a 10 kV accelerating voltage, image resolutions of 1500*1500 to 2500*2500 pixels, dwell times of 80.0 to 150.0 ms and a spot size of ~5.0 µm.

Zircon grains were examined for crystal-plastic deformation structures using orientation contrast images acquired with a forescattered-electron detector (FSD) mounted on the EBSD-tube of a FEI Quanta 3D FEG instrument (Faculty of Geosciences, Geography and Astronomy at the University of Vienna, Austria). For forward-scattered electron imaging the EBSD tube was retracted by ca. 5 mm in order to obtain maximum signal intensity on the FSD. The electron beam was used with a 15 kV accelerating voltage and a 2.5–4 nA probe current in analytic mode. The stage was tilted to 70° tilt at a 14–16 mm working distance.

3.2 Zircon micro- and nanostructure imaging by TEM

For transmission electron microscopy (TEM), three foils were prepared with the site-specific focused-ion-beam (FIB) technique that allows cutting of an electron-transparent foil from pre-selected areas of interest (Wirth, 2009). The foils are 15-20 µm wide, 10-15 µm deep and approximately 100 nm thick. A glass fiber attached to a micro-manipulator was used to lift foils out of their excavation sites. Images of the FIB foils are presented in Supplementary Figure 1. Details of the technique are given in Wirth (2004, 2009). Analytical and energy-filtered high-resolution transmission electron microscopy (ATEM, HRTEM) was conducted using a FEI Tecnai™ G2 F20 X-Twin at the GFZ Potsdam. The TEM operated at 200 kV using a field emission gun (FEG) electron source. It is equipped with a post-column Gatan imaging filter (GIF) Tridiem. The HRTEM images presented are energy-filtered using a 20 eV window on the zero loss peak. Analytical TEM was performed with an EDAX X-ray analyzer equipped with an ultra-thin window. The X-ray intensities were measured in scanning transmission mode (STEM), where the electron beam is serially scanned over a preselected area, minimizing mass loss during data acquisition. Fast Fourier

Transforms (FFT) from high-resolution images provided diffraction data. The D-spacings were calculated from diffraction pattern (FFT) of the high-resolution images.

3.3 U-Pb geochronology

Isotopic analyses of U, Th and Pb in zircon were carried out using a Sensitive High-Resolution Ion Microprobe (SHRIMP II) at the Korea Basic Science Institute (KBSI). Analysis spots were ca. 15 μm across, produced by a negative oxygen (O_2^-) beam of ions with a current of -5 nA on the sample surface. The reference zircon SL13 provided by the Australian National University (Ireland and Williams, 2003) was used for the calibration of the U concentrations (U = 238 ppm). The U-Pb ratios were corrected for instrumental intra-element fractionation using ratios measured on reference zircon FC1 with an age of 1099 Ma (Paces and Miller, 1993) with internal precision of 0.65% and external precision of 0.35% (2 sigma). Due to problems with overcorrection of ages using ^{204}Pb-based estimates of common Pb, ^{207}Pb-corrected U-Pb ages were used for population analysis. Analyses with high common Pb (>1%) are excluded from the dataset. Data reduction and processing was conducted using SQUID (version 2.50) and ISOPLOT (version 3.75) add-ins for Microsoft Excel, provided by K. R. Ludwig of the Berkeley Geochemistry Center of University of California (Ludwig, 2009, 2012). Data uncertainties include the spot-to-spot variation in standard analyses and the decay constant error.

4. RESULTS

4.1 Zircon nanostructure

Grain 14 consists of a small CL-dark detrital core (zone 1), an intermediate-CL metamorphic inner rim (zone 3), and a partial outer rim of high-CL metamorphic zircon (zone 4; Fig. 2A). No euhedral growth zoning is preserved in this grain. It is severely fractured, especially in its lower part. Orientation contrast imaging shows that the core region is composed of segments that are slightly misoriented against each other (mosaic crystal; Fig. 2D). Two sets of PDBs were identified in Kovaleva et al. (2015, Fig. 2C) based on EBSD mapping, and the direction of their traces is

shown in Fig. 2D. One set of PDBs runs horizontally across the grain, with the second running from lower right to upper left. The position of the FIB foil, across the zones 3 and 4, is highlighted by a white rectangle. The FIB foil in this grain was taken from metamorphic part of the zircon parallel to one of the PDB sets, which is parallel to the {100} crystallographic plane (Kovaleva et al., 2015).

The STEM imaging of the foil reveals straight parallel dislocation lines up to 3 μm long (Fig. 2B,C). Straight dislocation lines are characteristic for dislocation glide. These dislocations are distributed across the TEM foil. Curved dislocations and a few dislocation loops, indicating vacancy segregation, are also present (Fig. 3B*).* The dark spots on the HAADF (high-angle annular dark field image) are nano-pores. Figure 2C (HAADF) shows a low-angle grain boundary with an array of steeply inclined dislocations associated with fluid inclusions and pores (dark contrast) indicative of the presence of a fluid. The fluid in the pores was released during FIB milling. The occurrence of etch pits (inset in Fig. 2F) may indicate an earlier presence of fluids. Multiple fractures are also present. Dislocations usually continue through these cracks; an exception is shown in Figure 2E, where a variety of dislocation features (differing in orientations and type) occur on either side of the crack.

Grain 3b has a detrital core (zone 1) with concentric zoning, and a CL-bright rim (zone 4). Zircon is offset by a network of fractures, which run subvertically at the left-hand side (Fig. 3A,E). The offset left fragment is also fractured. Orientation contrast imaging (Fig. 3E) shows the presence of planar deformation bands, stretching diagonally from lower left to upper right, and a second set, stretching from lower right to upper left (for a structure characterization of the grain 3b refer to Kovaleva et al., 2015). The position of the FIB foil, across detrital core (zone 1), is highlighted by a white rectangle (Fig. 3A). The FIB foil is cut oblique to both documented sets of PDBs.

In the detrital core, dislocations are present with associated porosity (Fig. 3F, bright spots in the TEM bright field image pointed by arrows) and fluid inclusions (shown by arrows in Fig. 4B). The distribution of dislocation arrays is markedly different to that in grain 14 (Fig. 4). There are far fewer dislocations in the zircon lattice of grain 3b, with several discontinuous low-angle grain boundaries that have poorly arranged dislocation arrays. The distribution of dislocation arrays is heterogeneous across the foil.

The TEM imaging also reveals polyphase nanoinclusions composed of Pb-rich nanospheres 5-7 nm across, along with a Si-rich phase in some cases (Fig. 3C). The largest inclusion in Fig. 3C is composed of multiple phases, including Pb-rich nanospheres (brightest) and a slightly darker material containing Al, Na, S and Ca, that give the nanoinclusion a blurry appearance (Fig. 3D and H). The dark part of the nanoinclusion contains amorphous silica. High resolution imaging and EDS demonstrate that the nanospheres are composed of a crystalline Pb mineral (Fig. 3G). Diffraction patterns (FFT from high-resolution images) reveal d_{hkl} spacings corresponding to PbO (Table 1; for details see below).

In **Grain 17**, the CL image shows a detrital core with concentric growth zoning (zone 1), surrounded by a CL-intermediate metamorphic rim (zone 3) and a thin CL-bright outer rim (zone 4). The grain is slightly offset by a subvertical fracture at the right-hand side (Fig. 4A,E). Another healed fracture extends from the lower left to upper right and is decorated by fluid inclusions. Orientation contrast imaging reveals arrays of closely-spaced PDBs, stretching from lower left to upper right. For more details, see Kovaleva et al. (2015). The position of the FIB foil, across the CL-intermediate rim (zone 3) and detrital core (zone 1) is highlighted in the Figure 4A. The FIB foil was cut nearly perpendicular to the observed set of PDBs.

Bright field TEM images show porosity and dislocations concentrated along low-angle boundaries (Fig. 4B). Open fractures are present, along with others healed during annealing (Fig. 4C, darker area). The Zr/Si ratio from EDX spectra in the healed crack is slightly lower than in the host zircon (insets in the FIG 4C). Additionally, the dark area in the high-angle annular dark-field (HAADF) image (Fig. 4C) is slightly enriched in Mg, Al and Fe, as shown on the spectra. Lead oxide nanospheres up to 9 nm in diameter are present and are smaller and less abundant than those observed in previous studies (Kusiak et al., 2015, 2018; Whitehouse et al., 2017). The distribution of nanospheres does not show any relationship with the fractures or dislocation arrays. No Pb oxide nanospheres were observed inside the annealed fractures, as was the case with similar observation with zircon in Enderby Land (Kusiak et al., 2018). The EDX analysis reveal that nanoinclusions composed of Pb oxide also contain traces of Ti, Al and Ca. These polyphase inclusions commonly coexist with amorphous Si.

Crystallinity of the Pb oxide nanospheres was observed in both grains 3b and 17 (Figs. 3G and 4F). The d_{hkl} spacing of 4.65 Å and 2.95 Å show that the phase does not belong to cubic system as does native Pb or galena (PbS). These values agree well with the (001) and (200) d-spacings (4.754 Å and 2.948 Å, respectively) of PbO (Table 1).

4.2 Zircon grain characterization and U-Pb geochronology

Thirty analyses were performed on fifteen zircon grains. Zircons are 30 to 100 μm in diameter with round (Fig. 5A) and elongated (Fig. 5B) varieties. In CL images (see Supplementary Figure 2), most zircon grains show distinct detrital cores (marked as zone 1 in Fig. 5C) with concentric or sector growth zoning that is, in some cases, surrounded by a complex truncated and/or resorbed overgrowth (zone 2 in Fig. 5C). All grains have rounded outer rims of CL-bright zircon (zone 4 in Fig. 5C). In some grains, the cores are separated from high-CL outer rims by unzoned low-CL inner rims (zone 3 in Fig. 5C).

Excluding one analysis, high and low-CL rims (zones 3 and 4 accordingly) have lower Th/U (< 0.1) than detrital cores (0.2-0.8, Table 2). Of 29 analyses, eleven were excluded due to high common Pb content or acquisition on cracked, altered or inclusion-bearing zircon. The remaining 9 data points measured on both high and low-CL rims have similar ages, with higher-U analyses being slightly older. Together, high and low-CL rims yield a mean concordia age of 280.4 ± 3.9 Ma (n = 9; MSWD = 1.1; Fig. 6, inset). Texturally, the growth of zone 3 precedes zone 4; however, in this dataset, two generations are indistinguishable in age (Fig. 6, inset, low-U points color-coded light-blue, high-U color-coded yellow). Eight detrital cores (zone 1) yield U-Pb ages that scatter between 814 and 325 Ma, including three cores with a mean age of ca. 563 ± 2 Ma (n = 3; MSWD = 0.49); and one younger outlier (grain 3b presented on Fig. 3) of 185 ± 6 Ma attributed to Pb loss after metamorphism.

5. DISCUSSION

The formation, evolution and deformation of documented zircon proceeds as a response to geological events that affected the metapelitic host rock. Stages of growth with ages determined by SHRIMP provide the timing of metamorphism and

the provenance of detrital sources, and TEM observations demonstrate the effects of metamorphism on pre-existing zircon. Here, the evolution of zircon will be discussed with an assessment as to whether semi-brittle deformation producing PFs and PDBs have any effect on the preservation of radiogenic isotopic signatures.

All zircon grains studied revealed relatively CL-dark concentric-zoned cores (zone 1). Zircon with concentric euhedral and sector growth zoning is characteristic of growth within magma, and is therefore likely to have derived from the detrital sources of the metasediment (Fig. 5C, zone 1). Complex relationships between the margins of detrital cores (zone 2) and mantles CL-dark/intermediate zircon (zone 3) are characteristic of resorption and regrowth during metamorphism (e.g. Corfu et al., 2003). Zone 3 zircon is overgrown by CL-bright rims, typical of those found in high-grade metamorphic rocks (Corfu et al., 2003; Peressini et al., 2007). The growth of metamorphic rims on pre-existing zircon logically follows a stage of dissolution during prograde to peak metamorphism, with subsequent crystallization during post-peak cooling (Kohn et al., 2015). This implies that zircon rims in our sample (zones 3 and 4) started growing after peak metamorphism and continued growing during cooling from Zr-saturated metamorphic fluids and/or melts (e.g. Dempster et al., 2004; Hay and Dempster, 2009; Rasmussen, 2005).

Isotopic U-Pb analysis of zircon grains show detrital cores (zone 1) with a varied provenance (Fig. 5). Metamorphic zircon of both stages (zones 3-4) grew during a regional metamorphic event at ca. 280 Ma. The main physical difference in zircon between the metamorphic rims (zones 3 and 4) and detrital cores (zone 1) is that the latter were present before metamorphism and would have accumulated radiation damage prior to heating during metamorphism. The mottled diffraction contrast of the core of grain 3b (Fig. 3) indicates early stages of irradiation damage inducing amorphization followed by annealing caused by temperature increase during metamorphism. The continuous conflicting processes of diffraction damage and annealing producing similar mottled diffraction contrasts were already documented in monazite (Black et al., 1984; Seydoux-Guillaume et al., 2002, 2004).

The TEM observation revealed the presence of the Pb oxide nanospheres in detrital cores of the zircon grains but not in the rims. The nanospheres are smaller and less abundant than those observed in earlier studies. Moreover, the morphology of Pb oxide spheres differs significantly from those earlier documented in other geological

settings. In contrast to the native Pb nanospheres discovered in zircon from the UHT rocks in Enderby Land in East Antarctica (Kusiak et al., 2015; 2017) and the Kerala Khondalite Belt in Southern India (Whitehouse et al., 2017), the nanospheres found in zircon grains from the Ivrea-Verbano Zone are composed of Pb oxide. They usually occur as agglomerations of even smaller spheres together with other unknown phases that contain Al, Na and Fe. Because of differing compositions (not being just pure lead), these agglomerations of spheres lack sharp edges visible on native Pb spheres observed in previous studies. There is strong evidence that the Pb-oxide nanospheres are an assembly of much smaller pre-nucleation clusters of Pb-oxide thus forming a kind of mosaic crystal. It is not clear whether these elements (Al, Na, Fe) were in the zircon structure initially, or were brought in by metamorphic fluids that may also have oxidized the Pb. The presence of Pb-enriched domains on the nanoscale in high grade metamorphic rocks is not restricted to zircon. Earlier TEM studies describe similar features in monazite from polymetamorphic granulites of the Andriamena unit of Madagascar (Seydoux-Guillaume et al., 2003) and UHT Rogaland Complex of S Norway (Seydoux-Guillaume et al., 2018). Although no mineral phase was determined for Pb-enriched domains in those studies, such observations clearly show that Pb mobilization and nanoscale concentration may be common features of such rocks.

The semi-brittle to brittle deformation of zircon, and its relationship to the preservation of radiogenic Pb, can now be considered. Our TEM observations show that grain 17 has been fragmented, recrystallized, and subsequently healed, as indicated by the healed fracture (Fig. 4C). Zircon grain 14 was also fractured, partially healed and finally plastically deformed. Dislocations arranged in “micro-bands” similar to those shown in Fig. 2B,C (Grain 14) have been described in experimentally shocked zircon (Leroux et al. 1999). According to Leroux et al. (1999), “micro-bands” occupy {100} glide planes and possibly could act as precursors for planar fractures. Straight dislocations, as observed in our sample, indicate crystal-plastic deformation by dislocation glide without subsequent annealing. Dislocation loops, as observed in Fig. 2C, could have formed by vacancy segregation. The absence of annealing means that these deformation features formed after high-temperature metamorphism, which is consistent with the conclusions of Kovaleva et al. (2015). Dislocations which are straight and in glide configuration (Fig. 2B,C) are possibly

related to PDBs. Because the FIB foil was cut parallel to the plane of PDBs, dislocations might be a part of the latter, in which plane they are homogeneously distributed.

The Pb oxide nanospheres are present in annealed detrital cores only. No Pb nanospheres were observed in annealed fractures in detrital cores. However, we do observe them in the PDBs. Their distribution does not seem to be affected by crystal-plastic or brittle deformation features related to post-peak seismic/shearing events. It may still be the case that such deformed zircon is more susceptible to the loss of radiogenic Pb that was accumulated after deformation.

Zircon grains were fractured and deformed by seismic events, which postdate all zircon growth zones, including metamorphic rims of zones 3 and 4 (see also Kovaleva et al. 2015, Fig. 9a), possibly during the latest cooling stages of the ca. 280 Ma metamorphic event. One strongly deformed detrital core with PDBs (zircon 3b) yielded an apparent U-Pb age (185 Ma), younger than the metamorphism. This could be attributed to deformation of the zircon (Kovaleva and Klötzli, 2017) which make the crystal lattice more susceptible to Pb loss. However, metamorphic rims analysed by SHRIMP, for the most part, show no evidence of Pb loss. In addition, the preservation of Pb nanospheres produced by annealing during metamorphism in the detrital cores, also shows how radiogenic Pb has been preserved in zircon affected by brittle deformation.

Nanoscale concentrations of Pb observed by Kovaleva and Klötzli (2017) by NanoSIMS, were attributed to radiogenic Pb mobility in seismically deformed zircon. However, the new observations demonstrate the presence the Pb oxide nanospheres typical of those produces through the annealing of radiation damaged zircon during high grade metamorphism. No relationships between these Pb oxide nanospheres and brittle deformation features were observed.

5. CONCLUSIONS AND IMPLICATIONS

For the first time, we have provided a TEM study of zircon grains affected by deformation during late to post-metamorphic seismic activity, which contain Pb oxide nanospheres. The nanospheres were found in detrital zircon cores and not in metamorphic rims of the zircon grains. There is no clear relationship between the

distribution of Pb oxide nanospheres and PDBs and/or PFs, and therefore with the seismic event/s. Ages derived from metamorphic zircon show little evidence of Pb loss as a result of zircon deformation. Nanosphere formation occurred through thermal annealing during metamorphism, in detrital cores that had accumulated radiation damage. This is the first time the formation of lead oxide nanospheres has been documented, and also the first time Pb-bearing nanoinclusions have been observed in Phanerozoic rocks. This may be an indication that this little recognized nanoscale phenomenon may in fact be widespread in zircon from high-grade metamorphic rocks.

ACKNOWLEDGEMENTS

This research was performed thanks to the Alexander von Humboldt Fellowship awarded to MAK. EK is grateful to the National Research Foundation (NRF), grant #106511. Ian Lyon from Manchester University is thanked for numerous discussions. Thanks to Anja Schreiber from GFZ for FIB foils cutting and the Laboratory for scanning electron microscopy and focused ion beam applications, University of Vienna (Austria) for access to the EBSD technique, to Gerlinde Habler in particular. We thank A.J. Cavosie and an anonymous reviewer for detailed and valuable comments and the editor, C. Köberl for handing the manuscript.

References

Bea, F. and Montero, P. (2013) Diffusion-induced disturbances of the U–Pb isotope system in pre-magmatic zircon and their influence on SIMS dating. A numerical study. *Chem. Geol.* **349–350**, 1-17.

Bea, F., Montero, P. and Palma, J.F.M. (2018) Experimental evidence for the preservation of U-Pb isotope ratios in mantle-recycled crustal zircon grains. *Sci Rep-Uk* **8**, 12904.

Black, L.P., Fitz Gerald, J.D. and Harley, S.L. (1984) Pb Isotopic Composition, Color, and Microstructure of Monazites from a Polymetamorphic Rock in Antarctica. Contrib Mineral Petr 85, 141-148.

Bouvaist, J. and Weigel, D. (1970) Sesquioxyde de plomb, Pb2O3. I. Determination de la structure. *Acta Crystallographica Section A* **26**, 501-510.

Brodie, K.H. and Rutter, E.H. (1987) Deep crustal extensional faulting in the Ivrea Zone of Northern Italy. *Tectonophysics* **140**, 193-212.

Brodie, K.H., Rutter, E.H. and Rex, D. (1989) On the age of deep crustal extensional faulting in the Ivrea zone, northern Italy. *Geological Society, London, Special Publications* **45**, 203-210.

Cavosie, A.J., Erickson, T.M., Montalvo, P.E., Prado, D.C., Cintron, N.O. and Gibbon, R.J. (2018) The Rietputs Formation in South Africa: A Pleistocene fluvial archive of meteorite impact unique to the Kaapvaal craton, in: Moser, D.E., Corfu, F., Reddy, S.M., Darling, J., Tait, K. (Eds.), Microstructural Geochronology: Lattice to Atom-Scale Records of Planetary Evolution. AGU-Wiley, New Jersey, pp. 203-224.

Corfu, F. (2013) A century of U-Pb geochronology: The long quest towards concordance. *Geol. Soc. Am. Bull.* **125**, 33-47.

Corfu, F., Hanchar, J.M., Hoskin, P.W.O. and Kinny, P. (2003) Atlas of Zircon Textures. *Rev. Mineral. Geochem.* **53**, 469-500.

Davis, D.W., Williams, I.S. and Krogh, T.E. (2003) Historical development of zircon geochronology. *Rev. Mineral. Geochem.* **53**, 145-181.

Dempster, T.J., Hay, D.C. and Bluck, B.J. (2004) Zircon growth in slate. *Geology* **32**, 221-224.

Erickson, T.M., Cavosie, A.J., Moser, D.E., Barker, I.R. and Radovan, H.A. (2013) Correlating planar microstructures in shocked zircon from the Vredefort Dome at multiple scales: Crystallographic modeling, external and internal imaging, and EBSD structural analysis. *Am. Mineral.* **98**, 53-65.

Erickson, T.M., Cavosie, A.J., Pearce, M.A., Timms, N.E. and Reddy, S.M. (2016) Empirical constraints on shock features in monazite using shocked zircon inclusions. *Geology* **44**, 635-638.

Filatov, S., Bendeliani, N., Albert, B., Kopf, J., Dyuzeva, T. and Lityagina, L. (2005) High-pressure synthesis of α-PbO2 and its crystal structure at 293, 203 and 113 K from single crystal diffraction data. *Solid State Sci.* **7**, 1363-1368.

Garnier, P., Moreau, J. and Gavarri, J.R. (1990) Analyse de rietveld de la structure de Pb1-xTix01+x par diffraction des neutrons. *Mater. Res. Bull*. **25**, 979-986.

Gavarri, J.R. and Weigel, D. (1975) Oxydes de plomb. I. Structure cristalline du minimum Pb3O4, a temperature ambiante (293K). *J. Solid State Chem.* **11**, 344-345.

Ge, R., Wilde, S.A., Nemchin, A.A., Whitehouse, M.J., Bellucci, J.J., Erickson, T.M., Frew, A. and Thern, E.R. (2018) A 4463 Ma apparent zircon age from the Jack Hills (Western Australia) resulting from ancient Pb mobilization. *Geology* **46**, 303-306.

Geisler, T., Ulonska, M., Schleicher, H., Pidgeon, R.T. and van Bronswijk, W. (2001) Leaching and differential recrystallization of metamict zircon under experimental hydrothermal conditions. *Contrib. Mineral. Petr.* **141**, 53-65.

Guergouz, C., Martin, L., Vanderhaeghe, O., Thébaud, N. and Fiorentini, M. (2018) Zircon and monazite petrochronologic record of prolonged amphibolite to granulite facies metamorphism in the Ivrea-Verbano and Strona-Ceneri Zones, NW Italy. *Lithos* **308-309**, 1-18.

Hay, D.C. and Dempster, T.J. (2009) Zircon Behaviour during Low-temperature Metamorphism. *J. Petrol*. **50**, 571-589.

Ireland, T.R. and Williams, I.S. (2003) Considerations in zircon geochronology by SIMS. *Rev. Mineral. Geochem.* **53**, 215-241.

Kohn, M.J., Corrie, S.L. and Markley, C. (2015) The fall and rise of metamorphic zircon. *Am. Mineral.* **100**, 897-908.

Kovaleva, E. and Klötzli, U. (2017) NanoSIMS study of seismically deformed zircon: Evidence of Y, Yb, Ce and P redistribution and resetting of radiogenic Pb. *Am. Mineral.* **102**, 1311-1327.

Kovaleva, E., Klötzli, U., Habler, G., Huet, B., Guan, Y.B. and Rhede, D. (2017) The effect of crystal-plastic deformation on isotope and trace element distribution in zircon: Combined BSE, CL, EBSD, FEG-EMPA and NanoSIMS study. *Chemical Geology* **450**, 183-198.

Kovaleva, E., Klötzli, U., Habler, G. and Wheeler, J. (2015) Planar microstructures in zircon from paleo-seismic zones. *Am. Mineral.* **100**, 1834-1847.

Kunz, B.E., Regis, D. and Engi, M. (2018) Zircon ages in granulite facies rocks: decoupling from geochemistry above 850 °C? Contrib Mineral Petr 173, 26.

Kusiak, M.A., Dunkley, D.J., Wirth, R., Whitehouse, M.J., Wilde, S.A. and Marquardt, K. (2015) Metallic lead nanospheres discovered in ancient zircons. *Proc. Nat. Acad. Sci. of the United States of America* **112**, 4958-4963.

Kusiak, M.A., Whitehouse, M.J., Wilde, S.A., Dunkley, D.J., Menneken, M., Nemchin, A.A. and Clark, C. (2013a) Changes in zircon chemistry during Archean UHT metamorphism in the Napier Complex, Antarctica. *Am. J Sci.* **313**, 933-967.

Kusiak, M.A., Whitehouse, M.J., Wilde, S.A., Nemchin, A.A. and Clark, C. (2013b) Mobilization of radiogenic Pb in zircon revealed by ion imaging: Implications for early Earth geochronology. *Geology* **41**, 291-294.

Kusiak, M.A., Wilde, S., Wirth, R., Whitehouse, M.J., Dunkley, D.J., Lyon, I., Reddy, S.M., Berry, A.J. and de Jonge, M.D. (2018) Detecting micro- and nanoscale variations in element mobility in high-grade metamorphic rocks: implication for precise U-Pb dating of zircon, in: Moser, D.E., Corfu, F., Darling, J.R., Reddy, S.M., Tait, K. (Eds.), Microstructural Geochronology: Planetary Records Down to Atom Scale, Geophysical Monograph, First Edition ed. John Wiley & Sons, Inc., Am. Geoph. Union, pp. 279-292.

Leroux, H., Reimold, W.U., Koeberl, C., Hornemann, U. and Doukhan, J.C. (1999) Experimental shock deformation in zircon: a transmission electron microscopic study. *Earth Planet Sci. Lett.* **169**, 291-301.

Lide, D.R. (1983-84) Handbook of Chemistry and Physics. CRC Press.

Ludwig, K.R. (2009) Squid 2.5: A User's Manual. *Berkeley Geochronology Centre*, Berkeley, p. 104.

Ludwig, K.R. (2012) User's Manual for Isoplot 3.75. A Geochronological Toolkit for Microsoft Excel. *Berkeley Geochronology Center, Special Publication* **5**, p. 75.

Nasdala, L., Hanchar, J.M., Rhede, D., Kennedy, A.K. and Vaczi, T. (2010) Retention of uranium in complexly altered zircon: An example from Bancroft, Ontario. *Chemical Geology* **269**, 290-300.

Nasdala, L., Wenzel, M., Vavra, G., Irmer, G., Wenzel, T. and Kober, B. (2001) Metamictisation of natural zircon: accumulation versus thermal annealing of radioactivity-induced damage *Contrib. Mineral. Petrol*. **141**, 125-144.

Paces, J.B. and Miller, J.D.J. (1993) Precise U-Pb ages of Duluth Complex and related mafic intrusions, northeastern Minnesota: geochronological insights to physical, petrogenetic, paleomagnetic, and tectonomagmatic processes associated with the 1.1 Ga mid-continent rift system. *J. Geoph. Res*. **98**, 13998-14013.

Peressini, G., Quick, J.E., Sinigoi, S., Hofmann, A.W. and Fanning, M. (2007) Duration of a large Mafic intrusion and heat transfer in the lower crust: A SHRIMP U-Pb zircon study in the Ivrea-Verbano Zone (Western Alps, Italy). *J. Petrol.* **48**, 1185-1218.

Peterman, E.M., Reddy, S.M., Saxey, D.W., Snoeyenbos, D.R., Rickard, W.D.A., Fougerouse, D. and Kylander-Clark, A.R.C. (2016) Nanogeochronology of discordant zircon measured by atom probe microscopy of Pb-enriched dislocation loops. *Sci. Adv.* **2**, e1601318.

Piazolo, S., Austrheim, H. and Whitehouse, M.J. (2012) Brittle-ductile microfabrics in naturally deformed zircon: Deformation mechanisms and consequences for U-Pb dating. *Am. Mineral.* **97**, 154-156.

Piazolo, S., La Fontaine, A., Trimby, P., Harley, S., Yang, L., Armstrong, R. and Cariney, J.M. (2016) Deformation-induced trace element redistribution in zircon revealed using atom probe tomography. *Nat. Commun*. **7**, 20490.

Pittarello, L., Di Toro, G., Bizzarri, A., Pennacchioni, G., Hadizadeh, J. and Cocco, M. (2008) Energy partitioning during seismic slip in pseudotachylyte-bearing faults (Gole Larghe Fault, Adamello, Italy). *Earth Planet Sci. Lett.* **269**, 131-139.

Pittarello, L., Pennacchioni, G. and Di Toro, G. (2012) Amphibolite-facies pseudotachylytes in Premosello metagabbro and felsic mylonites (Ivrea Zone, Italy). *Tectonophysics* **580**, 43-57.

Rasmussen, B. (2005) Zircon growth in very low grade metasedimentary rocks: evidence for zirconium mobility at ~250 °C. *Contrib. Mineral. Petrol.* **150**, 146-155.

Reddy, S.M., van Riessen, A., Saxey, D.W., Johnson, T.E., Rickard, W.D.A., Fougerouse, D., Fischer, S., Prosa, T.J., Rice, K.P., Reinhard, D.A., Chen, Y. and Olson, D. (2016) Mechanisms of deformation-induced trace element migration in zircon resolved by atom probe and correlative microscopy. *Geochim. Cosmochim. Acta* **195**, 158-170.

Redler, C., Johnson, T.E., White, R.W. and Kunz, B.E. (2012) Phase equilibrium constraints on a deep crustal metamorphic field gradient: metapelitic rocks from the Ivrea Zone (NW Italy). *J. Metamorph. Geol*. **30**, 235-254.

Rubatto, D. (2017) Zircon: The Metamorphic Mineral. *Rev. Mineral. Geochem.* **83**, 261-295.

Rutter, E., Brodie, K., James, T. and Burlini, L. (2007) Large-scale folding in the upper part of the Ivrea-Verbano zone, NW Italy. *J. Struct. Geol*. **29**, 1-17.

Seydoux-Guillaume, A.M., Bingen, B., Paquette, J.L. and Bosse, V. (2015) Nanoscale evidence for uranium mobility in zircon and the discordance of U-Pb chronometers. *Earth Planet Sci. Lett.* **409**, 43-48.

Seydoux-Guillaume, A.-M., Wirth, R., Deutsch, A. and Schärer, U. (2004) Microstructure of 24-1928 Ma concordant monazites; implications for geochronology and nuclear waste deposits. Geochimica et Cosmochimica Acta 68, 2517-2527.

Seydoux-Guillaume, A.M., Wirth, R., Nasdala, L., Gottschalk, M., Montel, J.M. and Heinrich, W. (2002) An XRD, TEM and Raman study of experimentally annealed natural monazite. Phys Chem Miner 29, 240-253.

Timms, N.E., Kinny, P.D., Reddy, S.M., Evans, K., Clark, C. and Healy, D. (2011) Relationship among titanium, rare earth elements, U-Pb ages and deformation microstructures in zircon: Implications for Ti-in-zircon thermometry. *Chem. Geol.* **280**, 33-46.

Timms, N.E., Reddy, S.M., Gerald, J.D.F., Green, L. and Muhling, J.R. (2012) Inclusion-localised crystal-plasticity, dynamic porosity, and fast-diffusion pathway generation in zircon. J Struct Geol 35, 78-89.

Valley, J.W., Cavosie, A.J., Ushikubo, T., Reinhard, D.A., Lawrence, D.F., Larson, D.J., Clifton, P.H., Kelly, T.F., Wilde, S.A., Moser, D.E. and Spicuzza, M.J. (2014) Hadean age for a post-magma-ocean zircon confirmed by atom-probe tomography. *Nat. Geosci.* **7**, 219-223.

Valley, J.W., Reinhard, D.A., Cavosie, A.J., Ushikubo, T., Lawrence, D.F., Larson, D.J., Kelly, T.F., Snoeyenbos, D.R. and Strickland, A. (2015) Nano- and micro-geochronology in Hadean and Archean zircons by atom-probe tomography and SIMS: New tools for old minerals. *Am. Mineral.* **100**, 1355-1377.

Whitehouse, M.J., Kusiak, M.A., Wirth, R. and Ravindra Kumar, G.R. (2017) Metallic Pb nanospheres in ultra-high temperature metamorphosed zircon from southern India. *Miner. Petrol.* **111**, 467-474.

Wirth, R. (2004) Focused Ion Beam (FIB): A novel technology for advanced application of micro- and nanoanalysis in geosciences and applied mineralogy. *Eur. J. Mineral.* **16**, 863-876.

Wirth, R. (2009) Focused Ion Beam (FIB) combined with SEM and TEM: Advanced analytical tools for studies of chemical composition, microstructure and crystal structure in geomaterials on a nanometre scale. *Chem. Geol.* **261**, 217-229.

Zanetti, A., Giovanardi, T., Langone, A., Tiepolo, M., Wu, F.-Y., Dallai, L. and Mazzucchelli, M. (2016) Origin and age of zircon-bearing chromitite layers from the Finero phlogopite peridotite (Ivrea–Verbano Zone, Western Alps) and geodynamic consequences. Lithos 262, 58-74.

Figure Captions

Fig. 1. A. Schematic geological map of the Ivrea–Verbano Zone, Southern Alps. CL = Cremosina Line; IL = Insubric Line; CMBL = Cossato-Mergozzo-Brrissago Line; PL = Pogallo Line; HTSZ = high-temperature shear zone of the Anzola-Val Grande area. After Zanetti et al. (2016). B. Field photograph of the sampled outcrop above the road at Premosello, GPS coordinates: 46°00'23.65" 8°19'41.66". C. Microphotograph of the thin section, dark zone at the right – ultramylonite (black) with the pseudotachylite (dark-brown) in the center.

Fig. 2. Characteristic features of grain 14, as revealed by TEM; FIB foil #5086; A) CL image with white rectangle marking FIB foil cut; B,C,E and F) High-angle annular dark-field (HAADF) TEM images showing various features in zircon: B) dislocation lines (white) in glide configuration; straight and curved dislocation lines are present; examples of porosity connected with dislocations are marked by arrows; inset shows pore magnification; C) low angle grain boundary 'decorated' with fluid inclusion bubbles (pointed by arrows), black square shows location of the magnified image (F); D) orientation contrast image of grain 14 with dashed lines showing planar deformation bands (PDBs); E) subvertical fracture pointed by arrow; note the different orientations of dislocation at both sides of the crack; F) close up of image C displaying porosity connected with healed crack; inset in this image shows enlargement of etch pit. A) & D) after Kovaleva et al., 2015, modified.

Fig. 3. Characteristic features of grain 3b; as revealed by TEM; FIB foil #5087; A) CL image with white rectangle marking FIB foil cut; B and C) HAADF images: B) dislocation caused by fluid pressure; C) Pb spheres; D and H) EDS spectra documenting the presence of Pb, Si, Al, S and Ca; E) orientation contrast image of zircon; F) bright field (BF) image showing dislocation features and pores (white dots pointed by arrows); G) high resolution (HR) image of the Pb oxide nanosphere presented in (C) documenting its crystallinity. A) & D) after Kovaleva et al., 2015, modified.

Fig. 4. Characteristic features of grain 17; as revealed by TEM; FIB foil #5088; A) CL image with white rectangle marking FIB foil cut; B) bright field (BF) image showing low angle grain boundary, dislocations and crack in zircon; C) HAADF image of healed crack in zircon and EDS spectra inside the crack and within the zircon matrix; D) two Pb spheres (white dots) enclosed in Si (black area around white Pb); E) orientation contrast image; F) HREM image of Pb sphere from (D); G) EDS elemental spectrum documenting the presence of Pb oxide nanosphere. A) & D) after Kovaleva et al., 2015, modified.

Fig. 5. Cathodoluminescence (CL) images of selected grains used for geochronology; A) grain 4; B) grain 2; C) grain 9; zones marked on this grain: 1) inherited core; 2) resorption domain with remnant of oscillatory zoning; 3) CL black 'overgrowth', faintly patchy; 4) CL bright, high-T metamorphic overgrowth or recrystallization (white pests). All scale bars are 50 µm.

Fig. 6. Tera-Wasserburg Concordia diagrams for SHRIMP dating of zircon on sample IVZ-02-12. Inset: enlargement of ca. 280 Ma dataset being color-coded according to U content in the grain.

Table 1. D-spacing of analyzed Pb nanospheres compared with published values for native Pb and Pb oxides. Values in the first column were obtained in this study.

Table 2. SHRIMP U-Th-Pb zircon data from Ivrea-Verbano Zone.

Table 1. D-spacing of analysed Pb nanospheres compared with published values for native Pb and Pb oxides. Values in the first column were obtained in this study.

d_{hkl} observed [Å]	**Pb** cubic	**PbO** orthorhombic	**PbO_2** orthorhombic	**Pb_2O_3** monoclinic	**Pb_3O_4** tetragonal	**PbS** Cubic
	a_0 = 4.9505 Å	a_0 = 5.8952 Å b_0 = 5.9590 Å c_0 = 4.7544 Å	a_0 = 4.9858 Å b_0 = 5.6250 Å c_0 = 5.4626 Å	a_0 = 7.8140 Å b_0 = 8.8118 Å c_0 = 8.4650 Å ß = 124.97°	a_0 = 8.8118 Å b_0 = 8.8118 Å c_0 = 6.5639 Å	a_0 = 5.8936 Å
4.65 (001)	4.9505 (001)(010)	4.7544 (001)	4.9858 (100)	4.4294 (-102)	4.5185 (111)	3.429
2.95 (200)		2.9476 (200)	2.9795 (020)	2.9476 (200)	2.9034 (112)	2.969
	2.858 (111)	2.7465 (020)	2.7310 (002)	2.8125 (020)	2.7863 (310)	2.107
				2.7465 (020)		1.790
		2.4896 (120)	2.4929 (200)	2.4896 (120)	2.5216 (212)	1.714
	Lide 1983-1984	Garnier et al. 1990	Filatov et al. 2005	Bouvaist & Weigel 1975	Gavarri & Weigel 1975	JCPDS 5-592 Database

Table 2. SHRIMP U-Th-Pb zircon data from Ivrea-Verbano Zone; italic data were not considered in the age calculation due to the high common Pb content.

Spot	7-corr ppm $^{206}Pb^{*}$	ppm U	ppm Th	$^{232}Th/^{238}U$	±%	7-corr $^{204}Pb/^{206}Pb$	% $206Pb_c$	$^{207}Pb/^{206}Pb$	±%	$^{206}Pb/^{238}U$	±%	$^{206}Pb/^{238}U$ Age	
IVZ12_5.1	19.4	168	92	0.57	0.50	4.3E-4	0.75	0.073	2.3	0.595	2.5	814	±12
IVZ12_13.1	45.6	531	191	0.37	1.36	4.5E-4	0.79	0.067	2.3	0.450	1.5	615	±8
IVZ12_9.1	11.6	146	46	0.32	3.60	8.1E-5	0.14	0.060	2.0	0.371	4.5	570	±9
IVZ12_11.1	11.9	153	29	0.19	0.81	5.3E-4	0.95	0.066	1.9	0.387	1.5	558	±8
IVZ12_4.1	11.7	151	117	0.80	0.44	2.3E-4	0.42	0.062	6.8	0.398	1.5	556	±22
IVZ12_1.1	12.2	225	70	0.32	0.51	2.3E-4	0.42	0.058	1.8	0.261	0.7	393	±9
IVZ12_4.2	25.8	529	46	0.09	0.59	1.6E-5	0.03	0.054	2.6	0.247	2.4	357	±6
IVZ12_15.2	81.0	1824	534	0.30	0.28	8.5E-5	0.15	0.054	1.2	0.185	0.4	325	±5
IVZ12_9.2	18.4	459	7	0.02	1.63	2.1E-4	0.38	0.055	1.6	0.206	1.8	294	±5
IVZ12_3.1	19.9	498	10	0.02	1.29	-5.6E-5	--	0.051	3.4	0.197	1.7	293	±4
IVZ12_15.1	21.7	551	309	0.58	0.78	1.8E-4	0.32	0.055	1.7	0.150	2.2	290	±5
IVZ12_7.1	6.8	171	14	0.09	1.14	-6.0E-5	--	0.051	2.7	0.206	1.0	289	±4
IVZ12_8.1	8.9	232	10	0.04	1.34	-7.2E-5	--	0.051	2.4	0.194	0.9	283	±4
IVZ12_10.1	10.0	262	10	0.04	1.34	2.3E-4	0.43	0.055	2.1	0.198	2.8	280	±4
IVZ12_15.6	*8.2*	*216*	*175*	*0.84*	*0.55*	*2.9E-3*	*5.28*	*0.094*	*7.9*	*0.162*	*10.1*	*278*	*±27*
IVZ12_2.1	9.9	262	7	0.03	1.47	1.1E-4	0.21	0.054	3.7	0.155	0.8	278	±4
IVZ12_6.1	7.7	205	11	0.06	1.27	1.2E-4	0.21	0.054	2.6	0.177	2.8	278	±4
IVZ12_6.2	8.7	230	12	0.05	1.22	-4.4E-5	--	0.051	2.4	0.200	1.8	277	±4
IVZ12_15.3	*7.2*	*193*	*159*	*0.85*	*0.59*	*2.8E-3*	*5.08*	*0.093*	*12.2*	*0.160*	*8.2*	*276*	*±25*
IVZ12_15.9	*7.4*	*222*	*194*	*0.91*	*0.51*	*3.5E-3*	*6.35*	*0.102*	*2.8*	*0.140*	*3.2*	*245*	*±10*
IVZ12_15.10	*6.6*	*202*	*108*	*0.55*	*0.67*	*3.2E-3*	*5.95*	*0.099*	*3.2*	*0.140*	*1.4*	*239*	*±4*
IVZ12_15.4	*6.8*	*213*	*116*	*0.56*	*0.67*	*3.0E-3*	*5.57*	*0.095*	*3.5*	*0.135*	*4.1*	*235*	*±10*
IVZ12_15.5	*6.0*	*193*	*39*	*0.21*	*1.01*	*3.8E-3*	*6.98*	*0.107*	*11.0*	*0.143*	*4.0*	*230*	*±10*
IVZ12_12.1	27.4	915	158	0.18	0.35	4.2E-5	0.08	0.051	1.4	0.147	0.5	221	±3
IVZ12_3B	*17.7*	*710*	*82*	*0.12*	*0.61*	*6.7E-3*	*12.34*	*0.148*	*13.3*	*0.105*	*0.7*	*185*	*±6*
IVZ12_3B1	*7.0*	*285*	*117*	*0.42*	*0.89*	*5.9E-3*	*10.90*	*0.137*	*2.2*	*0.092*	*1.1*	*181*	*±3*

Errors are 1-sigma; Pb_c and Pb^{*} indicate the common and radiogenic portions, respectively.

Error in Standard calibration was 0.35% (not included in above errors but required when comparing data from different mounts).

Common Pb corrected using measured ^{207}Pb.

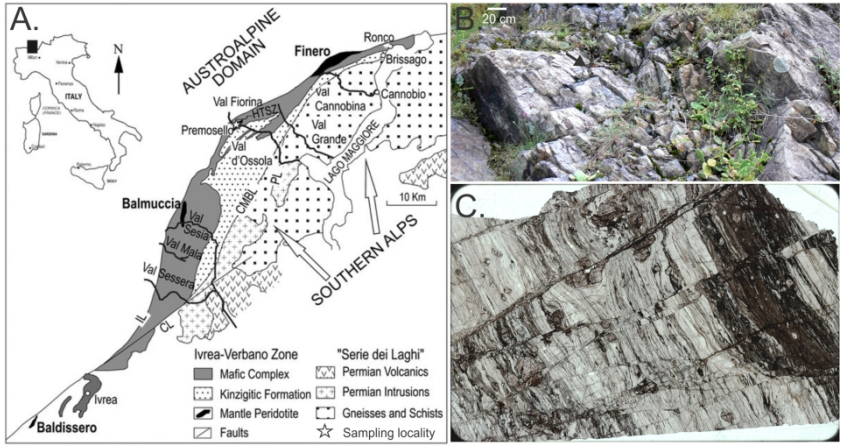

Fig. 2. Kusiak et al., Pb nanospheres in IVZ; R1

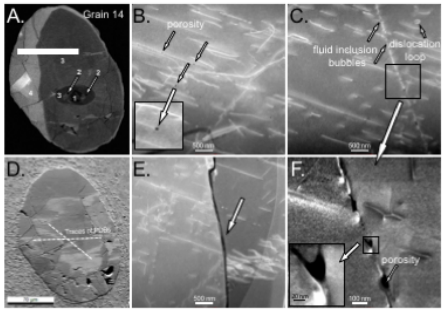

Fig. 3. Kusiak et al., Pb nanospheres in IVZ; R1

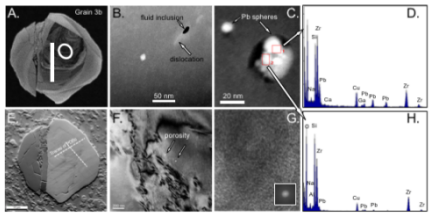

Fig. 4. Kusiak et al., Pb nanospheres in IVZ; R1

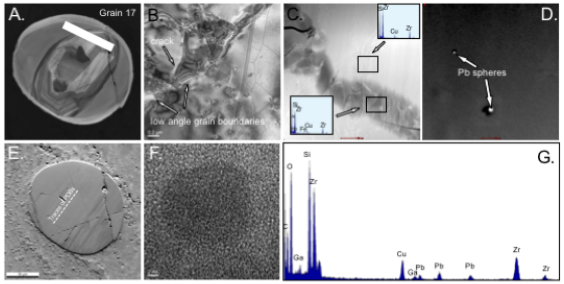

Fig. 5. Kusiak et al., Pb nanospheres in IVZ; R1

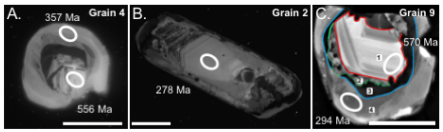

Fig. 6. Kusiak et al., Pb nanospheres in IVZ; R1_cor